Entrainment rate diurnal cycle in marine stratiform clouds estimated from geostationary satellite retrievals and a meteorological forecast model

David Painemal[1,2], Kuan-Man Xu[2], Rabindra Palikonda[1], and Patrick Minnis[1,2]

[1]Science Systems and Applications, Inc.
[2]NASA Langley Research Center

Abstract

The mean diurnal cycle of cloud entrainment rate (w_e) over the northeast Pacific region is for the first time computed by combining, in a mixed-layer model framework, the hourly-composited GOES-15 satellite-based cloud top height (H_T) tendency, advection, and large-scale vertical velocity (w) during May to September 2013, with horizontal winds and w taken from the ECMWF forecast model. The tendency term dominates the magnitude and phase of the w_e diurnal cycle, with a secondary role of w, and a modest advective contribution. The peak and minimum in w_e occur between 20:00-22:00 LT and 9:00-11:00 LT, respectively, in close agreement with the diurnal cycle of turbulence driven by cloud-top longwave cooling. Uncertainties in H_T and ECMWF fields are assessed with in-situ observations and three meteorological reanalysis datasets. This study provides the basis for constructing nearly-global climatologies of w_e by combining a suite of well-calibrated geostationary satellites.

1. Introduction

Cloud entrainment, the mixing of non-turbulent cloud-free air at the edges of the cloud layer, is a central mechanism governing cloud lifecycles within the cloud-topped marine boundary layer. Cloud top entrainment across the inversion base regulates the boundary layer turbulence, growth [*Lilly*, 1968], as well as the cloud cover and microphysical evolution in climatically important marine boundary layer regimes [*Wood*, 2012]. Thus, a proper parameterization of entrainment in climate models is paramount for simulating realistic cloud fields. Although entrainment rate measurements would be helpful for testing different entrainment closures in models, such estimates are scarce and limited to a few observational studies [*Wood et al.*, 2016].

Entrainment rates (w_e) from in-situ data are generally derived from aircraft measurements, by relating observed quantities to entrainment. Methods for estimating w_e include the use of the water budget equation, turbulence fluxes for conserved scalars near the inversion base, and the boundary layer (BL) mass budget equation in a mixed-layer model framework [e.g. *Bretherton et al.*, 1995; *Lenschow et al.*, 1999]. A shortcoming of these aircraft-based estimates is that direct comparisons with modeling results are difficult because the sparse aircraft sampling hinders a reliable estimation of climatologically representative entrainment rates. Among the different techniques for deriving w_e, the BL mass budget equation method is particularly appealing because the necessary measurements of inversion base or cloud top height are available from many ground-based sites equipped with radiosondes and cloud radars [e.g. *Caldwell et al.*, 2005; *Albrecht et al.*, 2016]. Moreover, satellite retrievals of cloud top height [e.g. *Zuidema et al.*, 2009] open the possibility of computing w_e at the regional or even global scale. Satellite-based w_e estimates were first attempted by *Wood and Bretherton* [2004] over the eastern Pacific by combining cloud top height retrievals based on two months of cloud temperature measurements from the MODerate resolution Imaging Spectroradiometer (MODIS), and horizontal winds and subsidence from the NCEP/NCAR Reanalysis. In their study, the w_e diurnal cycle was not estimated because the two sun-synchronous satellites that carry MODIS sensors (Terra and Aqua) are unable to sample the full diurnal cycle. As a result, their w_e was primarily modulated by the large-scale subsidence.

In this study, we describe a new approach to estimating entrainment rate for climate applications, using five months of hourly satellite data and meteorological outputs from a forecast model. More specifically, the boundary layer mass budget equation is utilized to estimate the diurnal cycle in entrainment rate in the subsidence region of the northeast Pacific domain during May to September of 2013, by combining cloud top height retrievals from the Fifteenth

Geostationary Operational Environmental Satellite (GOES-15) and meteorological fields simulated by the European Centre for Medium-Range Weather Forecasts (ECMWF) forecast model. Although the dataset enables the computation of instantaneous w_e, here we emphasize its diurnal cycle and regional pattern, with the goal of improving understanding of the large-scale processes that govern the variability in marine stratocumulus clouds. In addition, the use of composited fields help reduce random errors in the observations and in the ECMWF fields. Uncertainties in w_e are quantified by comparing GOES-15 and ECMWF meteorological fields against ship measurements from a recent campaign collected during the Marine ARM GPCI (Global Energy and Water Cycle Experiment –GEWEX- Cloud System Study –GCSS- Pacific Cross-section Intercomparison) Investigation of Clouds (MAGIC) field campaign [*Lewis and Teixeira*, 2015], and meteorological fields from three different reanalysis projects.

2. Dataset and Methodology

Even though entrainment rates can be calculated from the mass budget equation solely utilizing atmospheric model outputs, deficiencies in the model representation of the cloud-topped boundary layer, especially in the subtropics [e.g. *Dolinar et al.*, 2015] can propagate to the entrainment calculations. For the northeast Pacific region, *Malkus et al.* [2015] found that the ECMWF reanalysis underestimates the observed inversion base height during MAGIC. This is supported by Figure S1a, which shows ECMWF temperature profiles featuring weaker inversion gradients, and inversion bases 150 m lower than those from the MAGIC radiosondes.

Instead of relying on the ECMWF inversion height and cloud simuations, we utilize satellite cloud top height (H_T) estimated using an empirical relationship between cloud top and sea surface temperature, a technique that yields nearly unbiased retrievals [e.g. *Zuidema et al.*, 2009;

Sun-Mack et al., 2014]. Hourly retrievals of cloud top temperature (T_T) and cloud mask are derived from GOES-15 radiances at a nominal resolution of 4 km, utilizing the algorithms described in *Minnis et al.* [2008a, 2011], and further averaged to a 0.25˚ regular grid. In addition, surface contamination and the occurrence of high-level clouds are minimized by removing grids with cloud cover less than 90% and $T_T < 0$˚C. Daily sea surface temperature (*SST*) was taken from the Advanced Microwave Scanning Radiometer 2 AMSR-2 version 7 [*Wentz et al.*, 2010], at 0.25˚ resolution and averaged using a 3-day moving window (3-day product). H_T was calculated using the relationship in *Painemal et al.* [2013] derived from aircraft measurements over the southeast Pacific, and expressed as:

$$H_T = \frac{SST - T_T + 1.35}{0.0095} \quad [m] \qquad (1)$$

Although satellite H_T estimated using Eq. (1) compares well with aircraft data in the southeast Pacific [*Painemal et al.*, 2013] and the Cloud-Aerosol Lidar with Orthogonal Polarization (CALIOP) in the southeast Atlantic [*Painemal et al.*, 2015], we evaluate H_T against available shipborne radar observations collected between the port of Los Angeles California (33.7˚N, 118.2˚W) and Honolulu Hawaii (21.3˚N, 157.8˚W) during the MAGIC campaign from May to August of 2013. Cloud top height from the cloud radar was derived from the cloud mask in *Zhou et al.* [2015] after accounting for the radar altitude above sea level (approximately 20 m). The scatterplot between matched radar and satellite H_T for cloud tops lower than 2 km (Figure 1a) shows a good correspondence, with a linear correlation coefficient of 0.86, a positive bias of GOES-15 H_T of 27 m, and a root mean square difference (RMSD) of 178 m. Given the unique ability of GOES-15 to sample the full diurnal cycle, we also compared the satellite H_T composited diurnal cycle with the radar (Figure 1b). Both datasets agree in terms of phase, with maximum and minimum near 4:30 (±1.5 hours) and 16:30 (±1.5 hours), consistent with the expected diurnal cycle in marine stratocumulus clouds [e.g. *Painemal et al.*, 2013]. Even though the satellite H_T maximum is 63 m greater than that from the Ka-band cloud radar, the overall diurnal cycle amplitude for GOES-15 is only 42 m greater than its radar counterpart. The mean H_T map in Figure 1c shows the expected pattern for marine stratocumulus cloud regimes, that is, shallow cloud heights along the coast, and a progressive westward deepening [e.g. *Zuidema et al.* 2009; *Wood and Bretherton* 2004]. Moreover, the westward gradient, with values around 600 m near the coast and 1600 m near Hawaii (21˚N, 158˚W), agrees with radar and radiosondes observations reported by *Zhou et al.* [2015].

We compute w_e using the mixed-layer budget equation, expressed in terms of H_T as:

$$\frac{\partial H_T}{\partial t} + V \cdot \nabla H_T = w_e + w \qquad (2)$$

where V denotes the horizontal wind vector, ∇ the horizontal gradient operator, and w is the large-scale vertical velocity. Horizontal winds and vertical velocity fields are taken from the ECMWF forecast model operational in 2013 (cycles CY38R1 and CY38R2), using the forecast range from 12 to 36 hours (ECMWF 2017). Compared to standard reanalyses, the forecast model used here has the advantage of simulating fields at higher spatial and temporal resolutions with more realistic cloud fields free from spin-up effects, yet the forecast remains close to the initial conditions constrained by the analysis. The outputs are produced hourly, with a horizontal resolution of 0.5˚ degree and approximately 27 vertical levels below 2 km. Both hourly V and w are interpolated to the cloud top level (i.e. H_T). Vertical velocity at the cloud top is estimated from the pressure tendency using the hydrostatic equation and subtracting the near-surface level vertical velocity, as in *Wood and Bretherton* [2004] (this correction has a small impact in the final cloud-top vertical velocity). While our results are based solely on the ECMWF model, we show in Section 4 that the use of alternative meteorological datasets yield comparable results. To be consistent with the ECMWF fields resolution, the satellite H_T values are spatially averaged to 0.5° x 0.5°.

Since the final goal is to compute long-term averaged w_e, eq. (2) is hourly composited to yield:

$$< w_e >_i = \frac{\partial < H_T >}{\partial t}\bigg|_i + < V \cdot \nabla H_T >_i - < w >_i \qquad (3)$$

$$i = 0,1,2,..23\ hrs$$

where "$< >_i$" represents the hourly composite for the i^{th} time of the day. To remove noise in the tendency calculation, we first apply a 8-hour moving average to the H_T composite, and simultaneously fit a 12-hour and 24-hour cosine harmonics to the H_T diurnal cycle for each 0.5° grid, and expressed as:

$$H_T^*(t) = \overline{< H_T(t) >} + A_{24} \cdot \cos\left[\frac{2\pi}{24}(t - \phi_{24})\right] + A_{12} \cdot \cos\left[\frac{2\pi}{12}(t - \phi_{12})\right] \qquad (4)$$

$$i = 0,1,2,..23\ hrs$$

$\overline{< H_T(t) >}$ denotes the composite daily mean, whereas A and ϕ are, respectively, the amplitude and phase for each harmonic (12 and 24-hour). A cosine fit is justified by abundant evidence that shows that diurnal variations in cloud fraction, top height, divergence, and liquid water path in marine low clouds are well represented by a 24-hour cosine function, which is at times improved with the inclusion of a 12-hour harmonic [*Minnis and Harrison*, 1984; *Painemal et al.,* 2013; *Wood et al.*, 2009; *O'Dell et al.* 2009]. The high linear correlation (r) between H_T and H_T* in Figure 2a (blue and red crosses), with typical values ≥ 0.85, provides further justification for equation (4). It follows from Eq. (4) that the H_T tendency can be approximated as

$$\frac{\partial < H_T >}{\partial t}\bigg|_i \approx \frac{\partial H_T^*}{\partial t}\bigg|_i = -\frac{2\pi}{24} A_{24} \cdot \sin\left[\frac{2\pi}{24}(t - \phi_{24})\right] - \frac{2\pi}{12} A_{12} \cdot \sin\left[\frac{2\pi}{12}(t - \phi_{12})\right] \qquad (5)$$

The analytical expression in equation (5) simplifies the temporal derivative calculation, which is otherwise difficult given that the noise in the observations can yield spurious tendencies. Interestingly, results using equation (5) compare well with independent central differences calculations using the temporally smoothed H_T, with $r \geq 0.95$ over the region with the core of the stratocumulus cloud deck (Figure 2a, gray colors).

The advective term in Eq. (3) is calculated using the central difference formula, with the approximation: $< V \cdot \nabla H_T > \approx < V > \cdot < \nabla H_T >$. We found that this simplification is indeed adequate as the difference between $< V \cdot \nabla H_T >$ and $< V > \cdot \nabla < H_T >$ is small, with a mean bias of -0.07 cm s^{-1}, which is further reduced to -0.04 cm s^{-1} for regions with mean cloud fraction greater than 80%. These differences are negligible relative to the magnitude of entrainment rate, as we show in Section 3.

Finally, by combining Eqs. (3) and (5) we arrive at the following expression for entrainment rate:

$$< w_e >_i = \frac{\partial H_T^*}{\partial t}_i + < V > \cdot < \nabla_H H_T >_i - < w >_i \qquad (6)$$

Lastly, we reduced spatial noise by convoluting the advection and w in eq. (6), and H_T (prior to fitting the 12 and 24-hour harmonics) with a 5x5-grid moving Gaussian filter defined as $h = e^{-\frac{x^2+y^2}{2\sigma}}$. σ denotes the standard deviation of the distribution (σ=*2*-grids or 1˚*)*, and x and y are the distance (in grid boxes) from a specific latitudinal and longitudinal point ([-2 grids +2 grids]). The filter is further normalized by its total summation. Unlike the standard 5x5 spatial average, the Gaussian filter assigns a reduced weight to pixels farther from the moving 5x5 sub-matrix center.

3. Results

Figures 2b and c show two examples of diurnal cycles of the entrainment rate, tendency, advection, and vertical velocity terms of eq. (6). Measurements with a solar zenith angle between 75-88° (around ~18:00 LT and 06:00 LT) are not shown because they correspond to periods when the cloud mask algorithm transitions from its nighttime to daytime module (or vice versa), which produces at times subtle discontinuities. While this effect is generally small, removal of these samples should help reduce uncertainties in the satellite data. Values of w_e (Figures 2b and c, black lines) exhibit a diurnal cycle primarily explained by the H_T tendency ($\partial H_T^*/\partial t$, gray line). The entrainment rate diurnal cycle reaches its peaks around 21:00-23:00 LT, with values near 0.75 cm s^{-1} and 0.4 cm s^{-1} for the coastal and offshore regions, respectively. In contrast, minima occur near 8-11:00 LT, with magnitudes smaller than |-0.1 cm s^{-1}|. As we show in section 4, the negative values are within the uncertainty range of the calculations, although the inadequacy of the mixed-layer theory for some specific cases requires a closer consideration (Section 4). The advective term is generally small, with absolute values near 0.1 cm s^{-1}, and a subtle sign transition between coastal and offshore clouds (Figs. 2b and c, magenta). The figures also depict the excellent agreement between $< V >\cdot \nabla < H_T >$ and $< V \cdot \nabla H_T >$ (blue), which further corroborates the advective approximation in Eq. (6). The vertical velocity component, expressed as $-w$ (red lines) is typically positive (subsidence), as expected for a subtropical stratiform cloud regime, with values between 0.15 and 0.35 cm s^{-1}, and an unclear diurnal pattern.

Regional maps of w_e, subsidence ($-w$), and advective term are presented in Figure 3. As anticipated in Figures 2b and c, w_e has a strong diurnal cycle with a minimum around 10:00 LT and a maximum near 20:00 LT. Local maxima and minima reach magnitudes of 1.1 cm s^{-1} and -

0.3 cm s^{-1}, respectively, even though w_e is above -0.2 cm s^{-1} for most of the domain. Entrainment rates are greater east of 135°W, where the local maximum is found over the littoral zone north of 30°N. This coastal region is also characterized by strong subsidence and a diurnal cycle with maximum values of 0.6-0.7 cm s^{-1} in a region where the surface divergence is also a maximum [*Wood et al.*, 2009]. Over the rest of the domain, the diurnal variation in subsidence is mostly confined between 0.2 and 0.5 cm s^{-1}. Lastly, the advective term is small and mostly negatives, with values between -0.1 and 0.15 cm s^{-1}.

4. Discussion

We estimate the error associated with w_e using a Gaussian propagating error analysis. To quantify the H_T tendency error, we consider the RMSD for H_T of 178 m relative to the MAGIC cloud radar. Additionally, we take into account the spatial averaging of at least 20 samples (the combined effect of 0.5°x0.5° averaging and the Gaussian filter) and the composite of 60 hourly samples (average value from a total of 153 days), which reduce the H_T uncertainty to $\frac{178m}{\sqrt{20*60}} = \pm 5.1\ m$, and thus implying a tendency uncertainty of $\pm 5.1\ m\ hr^{-1} = \pm 0.14\ cm\ s^{-1}$. The vertical velocity uncertainty quantification is more challenging given the unavailability of w in-situ measurements. *Wood et al.* [2009] show that 850 hPa ECWMF ERA-Interim subsidence correlates well with satellite-derived surface divergence in the subtropics. In addition, the good agreement between matched ECMWF horizontal winds and MAGIC radiosondes in the lower troposphere (Figure S1b and c), suggests that the atmospheric circulation is properly represented in the model. It is interesting to note that issues with the ECMWF temperature inversion does not clearly affect the simulated circulation, a trait whose explanation is beyond the scope of this contribution. We attempt to further characterize uncertainties in ECMWF w by comparing it with independent modeling products. We used three well-known meteorological reanalysis datasets: the NCEP-DOE Reanalysis 2 (NCEP-R2) [*Kanamitsu et al.*, 2002], NASA's Modern-Era Retrospective analysis for Research and Applications, Version 2 (MERRA 2), [*Molod et al.*, 2015], and the Japanese 55-Year Reanalysis (JRA), [*Harada et al.*, 2016]. We compared daily vertical velocity at 850 hPa (~ 1.5 km), with the data interpolated to the NCEP-R2 spatial resolution (2.5˚x2.5˚), and subsampled every 6-hour (for ECMWF and MERRA-2) to emulate the NCEP-R2 time resolution. Time-averaged longitudinal sections for *w* at 35˚, 30˚, and 22˚N from ECMWF, NCEP-R2, MERRA-2, and JRA show a remarkably consistent pattern across the northeast Pacific (Figure 4). However, NCEP-2 departs from the other models near the coast, yielding stronger subsidence at 30˚N (Figure 4b). The agreement between ECMWF, MERRA-2, and JRA models is expected as they use more sophisticated data assimilation methods and higher spatial resolution than the NCEP-2 model [e.g. *Fujiwara et al.*, 2017]. Equivalent results are obtained when comparing *w* at 925 hPa (Figure S2). If one considers the RMSD for *w* between the ECMWF model and other reanalyses as a measure of model uncertainty, then the Gaussian uncertainty of the mean *w* (ε_w) is simply $\varepsilon_w = RMSD/\sqrt[2]{153}$, with 153 denoting the number of days. It is important to emphasize that ε_w is not the real uncertainty, however, the exercise of comparing ε_w using different reanalyses, provides insights into the error range expected from the meteorological models. The lower panels in Fig 4 (d, e, and f) depict ε_w between ECMWF and NCEP-R2, MERRA-2, and JRA, with typical ε_w encompassing values between 0.07-0.18 cm s^{-1}. Based on this range, we choose a conservative value, $\varepsilon_w = 0.13$ cm s^{-1}, for the uncertainty in subsidence, which is in agreement with the 25% error assessment in *Wood and Bretherton* [2004] (equivalent to 0.12 cm s^{-1} for $w=|0.5$ cm $s^{-1}|$). Given the small values of advection of less than |0.15| cm s^{-1}, we deem the error in advection to be negligible. It follows from the previous analysis that the uncertainty in w_e (δw_e) is the additive uncertainty of H_T tendency and w, that is, $\delta w_e = \pm(0.14 + 0.13)[cm\ s^{-1}] = \pm 0.27\ [cm\ s^{-1}]$. This uncertainty is up to four times smaller than the maximum w_e over the region, and yet similar in magnitude to the negative w_e in Figure 3. On the other hand, high negative w_e may also be reflecting the inadequacy of the mixed-layer model. For example, the location of the w_e negative minima in Figure 3 (upper panel, 19 UTC) with $w_e < -0.2$ cm s^{-1}, occur near the stratocumulus cloud domain edges. A closer look at the absolute value of the daily standard deviation in w normalized by its mean (coefficient of variation, Fig. S3), shows that regions with negative minima in w_e are concomitant with coefficient of variations greater than 2.0, that is, w variability relative to the mean is substantial. This suggests that in regions with strong synoptic variability and with frequent occurrence of positive w, the mixed-layer model inadequately represents the boundary layer dynamics.

Typical values of entrainment rates reported here are generally in agreement with aircraft-based w_e estimates near the coast of California during DYCOMS-II derived using four different datasets, with values between -0.22 and 0.7 cm s^{-1} [*Faloona et al.*, 2005]. Similarly, our satellite-based magnitudes also agree with radar-based entrainment rates over the ARM's Southern Great Plains site (0.0-1.1 cm s^{-1}) in *Albrecht et al.* [2016] but with an out-of-phase diurnal cycle that is likely associated with the dissimilar evolution of continental stratus, the focus of the *Albrecht et al.* [2015] study, relative to its maritime counterpart. Our results can be more closely compared to the ship-based analysis in *Caldwell et al.* [2005] over the southeast Pacific (20˚S, 85˚W) because both studies use a similar methodology for estimating the w_e diurnal cycle. The magnitude and phase similarities between the w_e diurnal cycle in the southeast Pacific [*Caldwell et al.,* 2005] and the offshore results in Figure 2c, highlight the boundary layer commonalities between both cloud regimes. In this regard, the satellite-based w_e diurnal cycle is concordant with the physics of marine stratocumulus clouds; with cloud thickening during the night and early morning that drives stronger cloud top longwave cooling, which in turns enhances turbulence and entrainment.

5. Summary

Five months of hourly-resolved GOES-15 cloud retrievals and AMSR2 SST, as well as ECMWF forecast model outputs, were used to estimate the entrainment rate over a vast region of the northeast Pacific using the mixed-layer boundary layer budget equation. Cloud top height was derived using a linear equation that relates the temperature differences between sea surface and cloud top temperatures with cloud height. Satellite-based H_T compares well with radar H_T during the MAGIC deployment, with a linear correlation of 0.86 and a mean bias of 27 m. H_T, advection, and vertical velocity from hourly ECMWF forecasts were hourly composited and the H_T tendency was further calculated by fitting a cosine function to the composited H_T diurnal cycle. We estimate a rough uncertainty in w_e of δw_e=±0.27 cm s^{-1}, with a small impact attributed to the choice of meteorological dataset utilized in the calculations. In fact, the good agreement between ECMWF, MERRA-2, and JRA lend confidence to the ability of numerical models to simulate robust circulation patterns in the northeast Pacific. Minima and maxima w_e occur at 9:00-11:00 and 20:00-22:00 local time respectively, with a diurnal cycle primarily explained by the cloud top height tendency. The w_e amplitude displays a clear spatial pattern with a local maximum of 1.1-1.2 cm s^{-1} along the California coast, where the subsidence is also strong, and a westward reduction to values of 0.3-0.4 cm s^{-1} at 155°W.

This is, to the best of our knowledge, the first time that hourly estimates of entrainment rates are attempted with satellite retrievals. Although the pioneering work by *Wood and Bretherton* [2004] reported entrainment rates using MODIS data, the cloud top height tendency could not be resolved, a term that explains most of w_e diurnal cycle in our study. Satellite-based computations of entrainment rate are likely less reliable in regions with cumulus clouds, where the boundary layer is more decoupled and surface fluxes become a more dominant source of turbulence. In addition, the method appears to yield more realistic results for the oceanic domain east of 140˚W, a region characterized by relatively strong subsidence and weak synoptic variability (Figure S3). It is encouraging that over a broad region, our results appear to be consistent with the diurnal cycle of turbulence driven by cloud-top longwave cooling, which is expected to dominate the diurnal cycle of entrainment rate. The satellite-based w_e introduced in this work can be used together with other aircraft and ground-based observations to understand the limitations of different methods of entrainment rate estimation [*Wood et al.*, 2016]. Lastly, ongoing efforts to retrieve cloud properties using inter-calibrated satellite radiances from different geostationary platforms [e.g. *Minnis et al.*, 2008b] offer the opportunity to estimate nearly global entrainment rates over the ocean and develop climatologies that could provide valuable information to the modeling community as well as helping further advance our knowledge of climatically relevant marine low clouds.

Acknowledgments: D. Painemal and Patrick Minnis were supported by the U.S. Department of Energy, Office of Biological and Environmental Research, Atmospheric System Research Program award # DESC0011675*, and CERES program. GOES-15 data are available at https://satcorps.larc.nasa.gov or upon request. AMSR2 data used in this study are produced by Remote Sensing Systems (RSS) and sponsored by the NASA Earth Science Physical Oceanography Program (available at www.remss.com). NCEP_Reanalysis 2 data are provided by the NOAA/OAR/ESRL PSD, Boulder, Colorado, USA, at http://www.esrl.noaa.gov/psd. MERRA-2 was obtained from the NASA Goddard Earth Science Data and Information Services Center at https://disc.gsfc.nasa.gov. The Japanese 55-year Reanalysis (JRA-55) project, carried out by the Japan Meteorological Agency (JMA), was downloaded from the Research Data Archive at the National Center for Atmospheric Research, Computational and Information Systems Laboratory. https://doi.org/10.5065/D6HH6H41.*

We are indebted of Dr. Maike Ahlgrimm from ECMWF for providing the forecast model outputs. Early discussions with Dr. Virendra Ghate from Argonne National Laboratory provided the motivation for exploring the use of geostationary data for entrainment rate calculations.

References

Albrecht, B., M. Fang, and V. Ghate (2016), Exploring Stratocumulus Cloud-Top Entrainment Processes and Parameterizations by Using Doppler Cloud Radar Observations, *J. Atmos. Sci.*, 73, 729–742, doi: 10.1175/JAS-D-15-0147.1.

Bretherton, C., P. Austin, and S. Siems (1995), Cloudiness and Marine Boundary Layer Dynamics in the ASTEX Lagrangian Experiments. Part II: Cloudiness, Drizzle, Surface Fluxes, and Entrainment, *J. Atmos. Sci.*, 52, 2724–2735, doi: 10.1175/1520-0469(1995)052<2724:CAMBLD>2.0.CO;2.

Caldwell, P., C. Bretherton, and R. Wood (2005), Mixed-Layer Budget Analysis of the Diurnal Cycle of Entrainment in Southeast Pacific Stratocumulus. J. Atmos. Sci., 62, 3775–3791, doi: 10.1175/JAS3561.1.

Dolinar, E. K., X. Dong, and B. Xi (2015), Evaluation and intercomparison of clouds, precipitation, and radiation budgets in recent reanalyses using satellite-surface observations, *Clim. Dyn.*, doi:10.1007/s00382-015-2693-z.

ECMWF 2017: IFS documentation, accessed March 2017, ECMWF. [Available online at http://www.ecmwf.int/en/forecasts/documentation-and-support/changes-ecmwf-model.]

Faloona, I., D. Lenschow, T. Campos, B. Stevens, M. van Zanten, B. Blomquist, D. Thornton, A. Bandy, and H. Gerber (2005), Observations of Entrainment in Eastern Pacific Marine Stratocumulus Using Three Conserved Scalars, *J. Atmos. Sci.*, 62, 3268–3285, doi: 10.1175/JAS3541.1.

Fujiwara, M., and co-authors (2017), Introduction to the SPARC Reanalysis Intercomparison Project (S-RIP) and overview of the reanalysis systems, *Atmos. Chem. Phys.*, 17, 1417-1452, doi:10.5194/acp-17-1417-2017.

Harada, Y., H. Kamahori, C. Kobayashi, H. Endo, S. Kobayashi, Y. Ota, H. Onoda, K. Onogi, K. Miyaoka, and K. Takahashi, 2016: The JRA-55 Reanalysis: Representation of atmospheric circulation and climate variability, *J. Meteor. Soc. Japan*, **94**, 269-302, doi:10.2151/jmsj.2016-015.

Kalmus P., S. Wong, and J. Teixeira (2015), The Pacific Subtropical Cloud Transition: A MAGIC Assessment of AIRS and ECMWF Thermodynamic Structure, *IEEE Geoscience and Remote Sensing Letters*, vol. 12, no. 7, pp. 1586-1590, doi: 10.1109/LGRS.2015.2413771.

Kanamitsu, M., W. Ebisuzaki, J. Woollen, S. Yang, J. Hnilo, M. Fiorino, and G. Potter (2002), NCEP–DOE AMIP-II Reanalysis (R-2), *Bull. Amer. Meteor. Soc.*, 83, 1631–1643, doi: 10.1175/BAMS-83-11-1631.

Lenschow, D. H., P. B. Krummel, and S. T. Siems (1999), Measuring entrainment, divergence, and vorticity on the mesoscale from aircraft. *J. Atmos. Oceanic Technol.*, 16, 1384–1400.

Lewis, E. R., and J. Teixeira (2015), Dispelling clouds of uncertainty, *Eos*, 96, doi:10.1029/2015EO031303.

Lilly, D. K. (1968), Models of cloud-topped mixed layers under a strong inversion, *Quart. J. Roy. Meteor. Soc.*, 94, 292–309.

Minnis, P. and E. F. Harrison (1984), Diurnal variability of regional cloud and clear-sky radiative parameters derived from GOES data, Part II: November 1978 cloud distributions, *J. Clim. Appl. Meteorol.*, *23*, 1012-1031.

Minnis P., and Coauthors (2008a), Cloud detection in non-polar regions for CERES using TRMM VIRS and Terra and Aqua MODIS data. IEEE Trans, *Geosci. Remote Sens.*, 46, 3857–3884.

Minnis, P., and Coauthors (2008b), Near-real time cloud retrievals from operational and research meteorological satellites, *Proc. SPIE Remote Sens. Clouds Atmos. XIII*, Cardiff, Wales, UK, 15-18 September, 7107, 7107-2, 8 pp., ISBN: 9780819473387

Minnis P., and Coauthors (2011), CERES edition-2 cloud property retrievals using TRMM VIRS and Terra and Aqua MODIS data—Part I: Algorithms. IEEE Trans, *Geosci. Remote Sens.*, 49, 4374–4400, doi:10.1109/TGRS.2011.2144601.

Molod, A., L. Takacs, M. Suarez, J. and Bacmeister (2015), Development of the GEOS-5 atmospheric general circulation model: evolution from MERRA to MERRA2, *Geosci. Model Dev.*, 8, 1339-1356, doi:10.5194/gmd-8-1339-2015.

O'Dell, C. W., F. J. Wentz, and R. Bennartz (2008), Cloud liquid water path from satellite-based passive microwave observations: A new climatology over the global oceans, *J. Climate*, **21**, 1721–1739, doi:10.1175/2007JCLI1958.1.

Painemal D., P. Minnis, and L. O'Neill (2013), The diurnal cycle of cloud-top height and cloud cover over the Southeastern Pacific as observed by GOES-10, *J. Atmos. Sci.*, 70, 2393–2408.

Painemal D., K-M Xu, A. Cheng, P. Minnis, and R. Palikonda (2015), Mean structure and diurnal cycle of Southeast Atlantic boundary layer clouds: Insights from satellite observations and multiscale modeling framework simulations, *J. Climate*, 28, 324–341.

Sun-Mack, S., P. Minnis, Y. Chen, S. Kato, Y. Yi, S.C. Gibson, P.W. Heck, and D.M. Winker (2014), Regional Apparent Boundary Layer Lapse Rates Determined from CALIPSO and MODIS Data for Cloud-Height Determination. *J. Appl. Meteor. Climatol.,* **53**, 990–1011, doi: 10.1175/JAMC-D-13-081.1.

Wood, R., and C. S. Bretherton, (2004), Boundary layer depth, entrainment, and decoupling in the cloud-capped subtropical and tropical marine boundary layer. *J. Climate*, 17, 3576–3588.

Wood R., M. Kohler, R. Bennartz, and C. O'Dell (2009), The diurnal cycle of surface divergence over the global oceans, *Quart. J. Roy. Meteor. Soc.*, 135, 1484–1493.

Wood, R. (2012), Stratocumulus Clouds, *Mon. Wea. Rev.*, 140, 2373–2423, doi: 10.1175/MWR-D-11-00121.1.

Wood, R., M. Jensen, J. Wang, C. Bretherton, S. Burrows, A. Del Genio, A. Fridlind, S. Ghan, V. Ghate, P. Kollias, S. Krueger, R. McGraw, M. Miller, D. Painemal, L. Russell, S. Yuter, and P. Zuidema (2016), Planning the Next Decade of Coordinated Research to Better Understand and Simulate Marine Low Clouds, *Bull. Amer. Meteor. Soc.*, 97, 1699–1702, doi: 10.1175/BAMS-D-16-0160.1.

Zhou, X., P. Kollias, and E. Lewis (2015), Clouds, precipitation and marine boundary layer structure during MAGIC, *J. Climate*, doi:10.1175/JCLI-D-14-00320.1.

Zuidema P., D. Painemal, S. de Szoeke, and C. Fairall (2009), Stratocumulus cloud top estimates and their climatic implications, *J. Clim.*, 22, 4652–4666, doi:10.1175/2009JCLI2708.1.

Figures

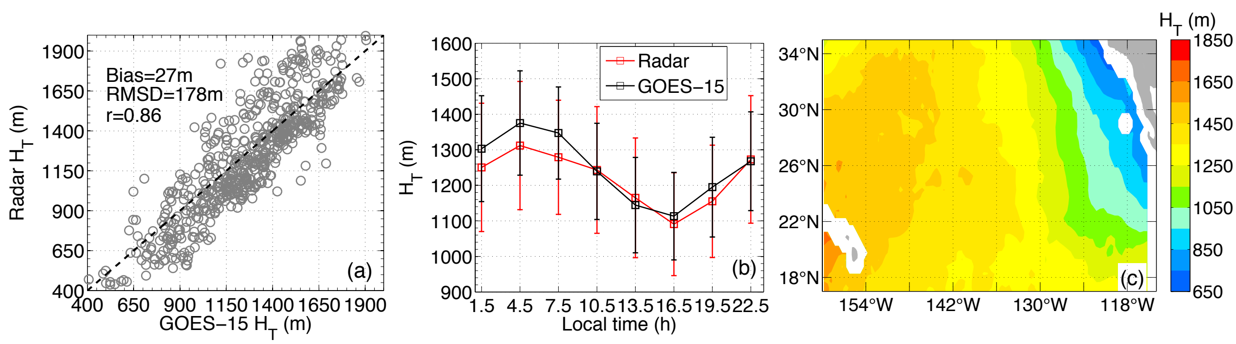

Figure 1: a) Scatterplot between satellite-based and MAGIC radar H_T values. b) H_T diurnal cycle from the MAGIC radar (red line) and collocated satellite H_T (black line). Vertical error-bars denote the standard deviation. Each averaged bin in Figure 1b contains at least fifty samples. c) Mean H_T map during the period of study.

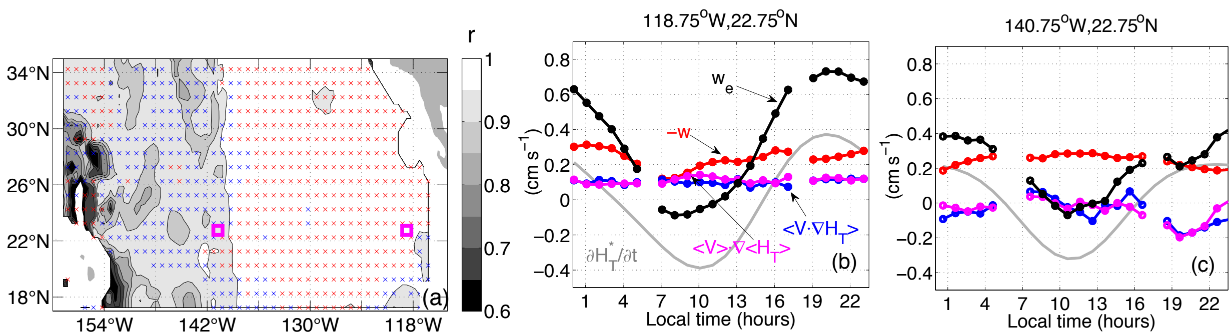

Figure 2: (a) Linear correlation (r) between: H_T* and H_T (red and blue crosses represent 0.93 > r ≥ 0.85 and r ≥ 0.93, respectively), and the tendency derived from H_T* and calculated using H_T central differences after applying a 8-hour moving average (gray shading). Diurnal cycles for (b) a coastal (118.75˚W, 22.75˚N) and (c) an offshore region (140.75˚W, 22.75˚N) denoted by the magenta squares in Figure 2a. w_e (black), w (red), $\frac{\partial H_T^*(t)}{\partial t}$ (gray), $< V \cdot \nabla H_T >$ (blue), and $< V > \cdot \nabla < H_T >$ (magenta).

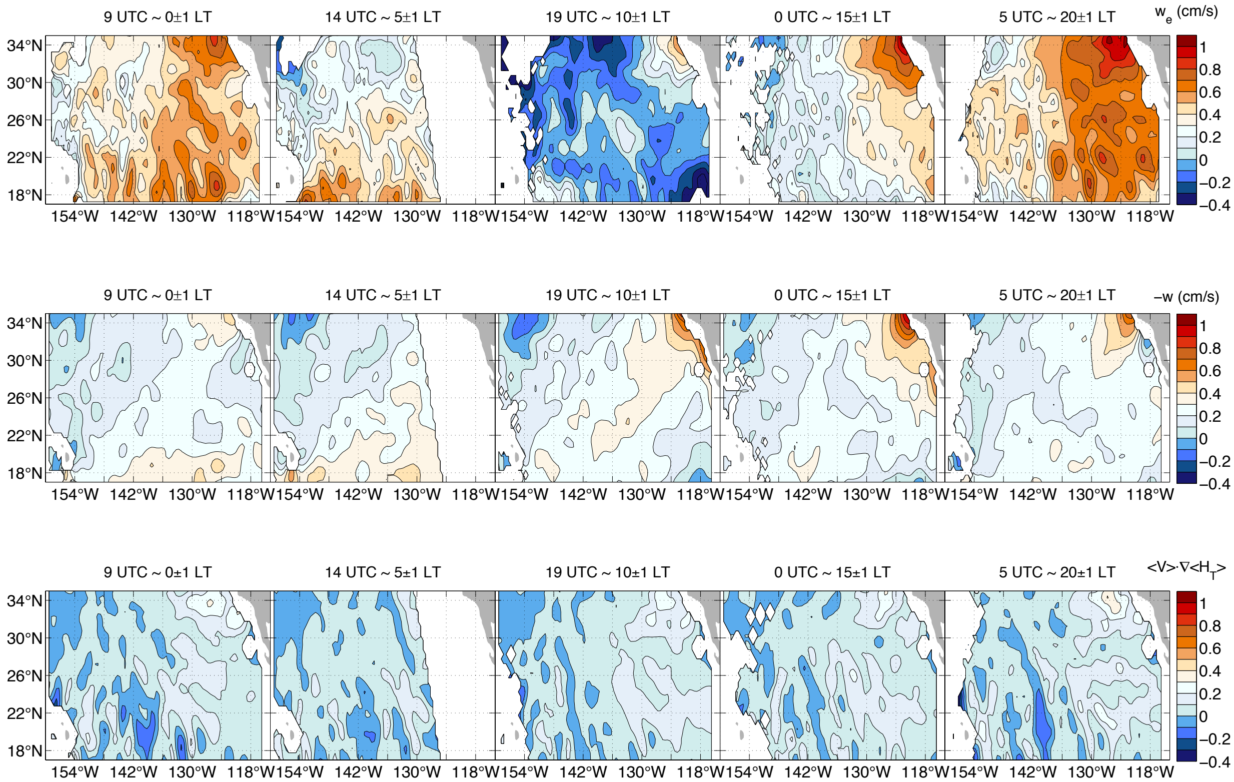

Figure 3: Entrainment rate (w_e, upper panel), subsidence ($-w$, middle panel), and advective term (lower panel) from eq. (6). w_e is only shown for regions with mean $-w>0$ (subsidence).

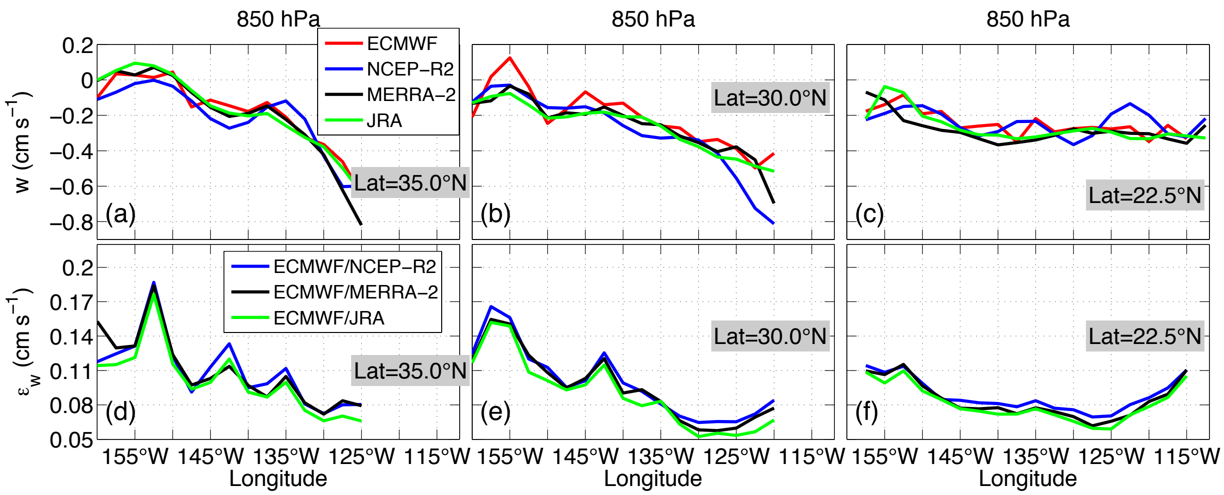

Figure 4: *w* at 850 hPa for three zonal transects from the ECMWF forecast model (red), NCEP-R2 (blue), MERRA-2 (black) and JMA (green) at (a) 35˚N, (b) 30˚N, and (c) 22.5˚N. Uncertainty proxy (ε_w) derived from the RMSD between ECMWF: and NCEP-R2 (blue), MERRA-2 (black) and JRA (green) at (d) 35˚N, (e) 30˚N, and (f) 22.5˚N

Auxiliary material for:

Entrainment rate diurnal cycle in marine stratiform clouds estimated from geostationary satellite retrievals and a meteorological forecast model

David Painemal, Kuan-Man Xu, Rabindra Palikonda, and Patrick Minnis

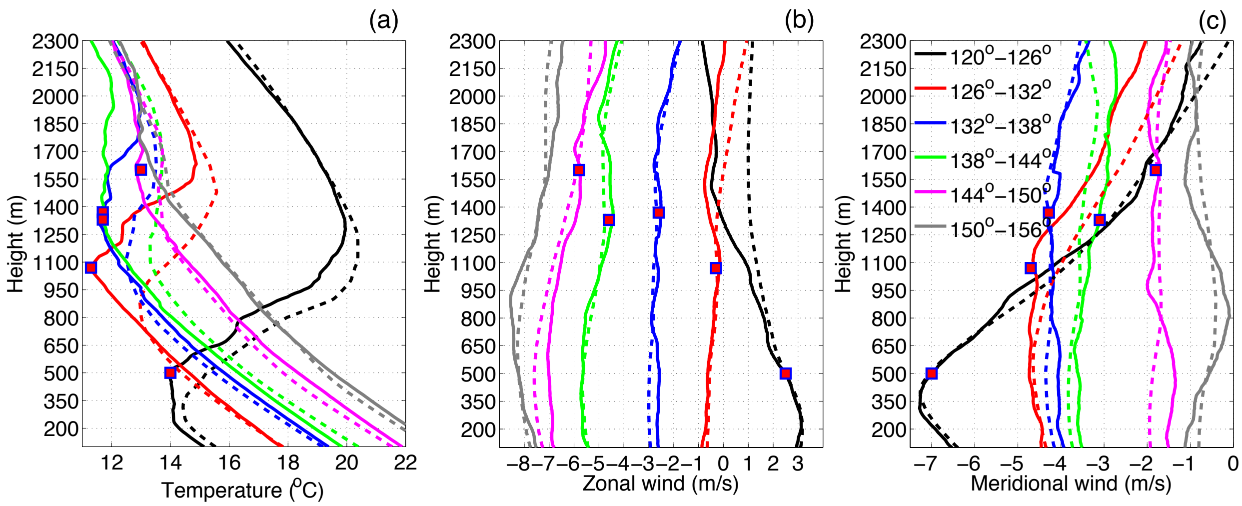

Figure S1: ECMWF vertical profiles collocated in time and space with MAGIC radiosondes, and further averaged along the MAGIC ship transect in six 6˚ longitudinal portions from May to September 2013. a) air temperature, zonal (b) and meridional wind (c) profiles. Blue squares denote the radiosonde-based mean inversion base height.

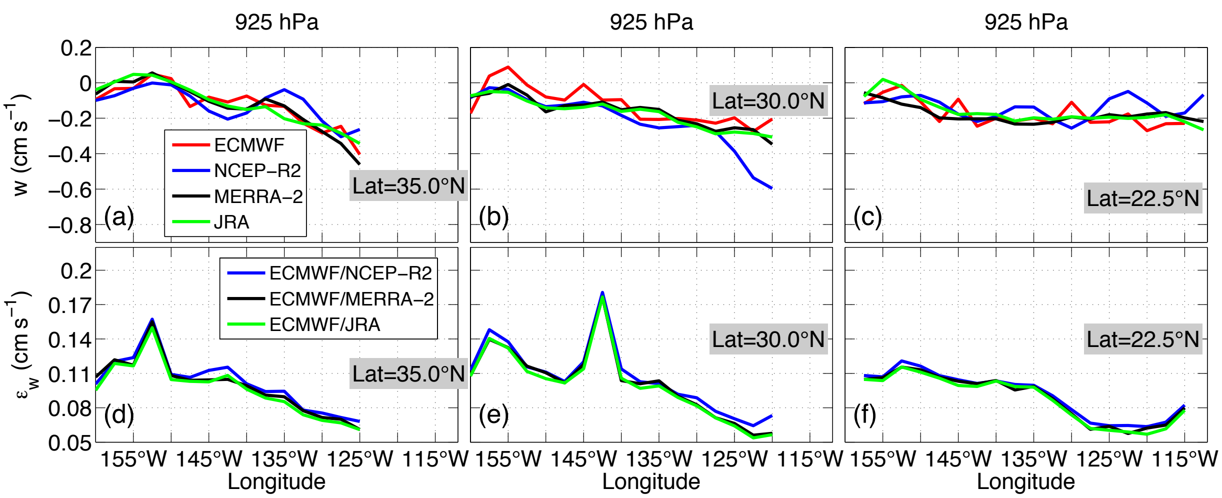

Figure S2: *w* at 925 hPa for three zonal transects from the ECMWF forecast model (red), NCEP-R2 (blue), MERRA-2 (black) and JMA (green) at (a) 35˚N, (b) 30˚N, and (c) 22.5˚N. Uncertainty proxy (ε_w) derived from the RMSD between ECMWF: and NCEP-R2 (blue), MERRA-2 (black) and JRA (green) at (d) 35˚N, (e) 30˚N, and (f) 22.5˚N

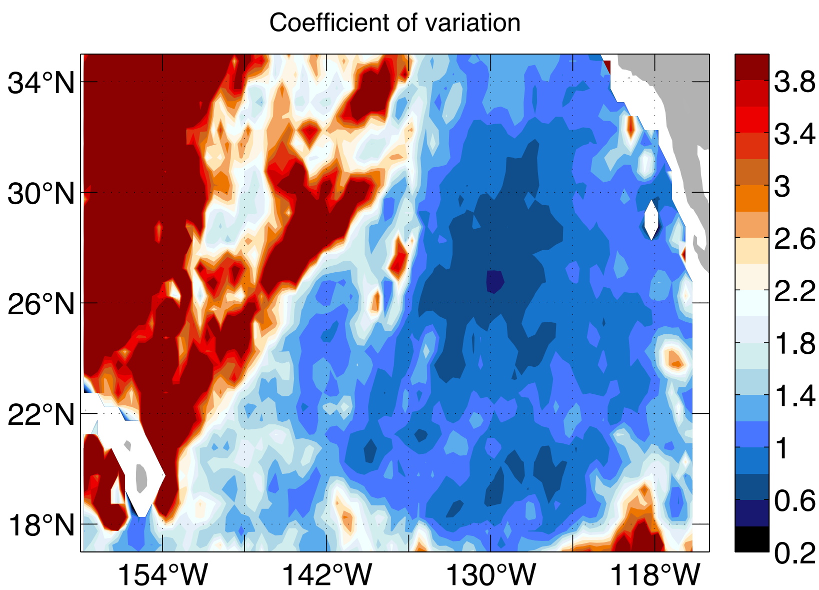

Figure S3: Coefficient of variation estimated using daily mean cloud top ECMWF vertical velocity during the period of study. The color scale saturates for values greater than 4.0.